NANO · MICRO small
www.small-journal.com

Ultralow-Overpotential Acidic Oxygen Evolution Reaction Over Bismuth Telluride–Carbon Nanotube Heterostructure with Organic Framework

Alvira Ayoub Arbab, Sehyeon Cho, Euibeen Jung, Hyun Soo Han, Sangwook Park, and Hyoungsoon Lee**

The state-of-the-art iridium and ruthenium oxides-based materials are best known for high efficiency and stability in acidic oxygen evolution reaction (OER). However, the development of economically feasible catalysts for water-splitting technologies is challenging by the requirements of low overpotential, high stability, and resistance of catalysts to dissolution during the acidic oxygen evolution reaction . Herein, an organometallic core–shell heterostructure composed of a carbon nanotube core (CNT) and bismuth telluride (Bi_2Te_3) shell (denoted as nC–Bi_2Te_3) is designed and use it as a catalyst for the acidic OER. The proposed catalyst achieves an ultralow overpotential of 160 mV at 10 mA cm^{-2} (geometrical), thereby outperforming most of the state-of-the-art precious-metal-based catalysts. The low Tafel slope of 30 mV dec^{-1} and charge transfer resistance (R_{CT}) of 1.5 Ω demonstrate its excellent electrocatalytic activity. The morphological and chemical compositions of nC–Bi_2Te_3 enable the generation of —OH functional group in the Bi—Te sections formed via a ligand support, which enhances the absorption capacity of H^+ ions and increases the intrinsic catalytic activity. The presented insights regarding the material composition–structure relationship can help expand the application scope of high-performance catalysts.

1. Introduction

Hydrogen (H_2) production is a vital and real-world solution for the global energy crises because H_2 gas is the most effective alternative to fossil fuels.[1] A proton-exchange membrane water electrolysis (PEMWE) system, in which the anodic (OER and cathodic hydrogen evolution reaction (HER) occur, is globally recognized as a sustainable and eco-friendly system for fuel generation.[2] Consequently, such systems are widely applied in renewable energy conversion and storage devices.[3] The acidic OER, which is a half-cell reaction of water splitting occurring at the anode, involves an undesirable, complex multistep proton-coupled charge transfer process owing to the high overpotential, low stability resulting from extraordinarily oxidative conditions, and slow kinetics of the OER. In acidic water splitting systems, precious metal oxides such as Pt, IrO_2, and RuO_2 are typically used as OER electrocatalysts.[4] However, RuO_2 and IrO_2, which are expensive and unstable at high anodic potentials (1.8–2.2 V) easily oxidize the catalysts in low-pH electrolytes, which renders the catalysts vulnerable to dissolution during the OER.[5]

Recently, bulk conductive heterostructures of carbon nanotubes (CNTs) have attracted considerable attention as catalysts for the half-cathodic HER in both acid and alkaline water splitting scenarios.[6] As a key member of the graphitic carbon

A. A. Arbab, H. Lee
School of Mechanical Engineering
Chung-Ang University
Seoul 06974, South Korea
E-mail: leeh@cau.ac.kr
S. Cho, E. Jung, H. Lee
Department of Intelligent Energy and Industry
Chung-Ang University
Seoul 06974, South Korea
H. S. Han
Department of Mechanical Engineering
Stanford University
Stanford, CA 94305, USA
The ORCID identification number(s) for the author(s) of this article can be found under https://doi.org/10.1002/smll.202307059

DOI: 10.1002/smll.202307059

H. S. Han
Department of Materials Science and Engineering
Stanford University
Stanford, CA 94305, USA
S. Park
Department of Mechanical Engineering
Seoul National University
Seoul 08826, South Korea
E-mail: swparkk1@snu.ac.kr
S. Park
Institute of Advanced Machines and Design
Seoul National University
Seoul 08826, South Korea
S. Park
Institute of Engineering Research
Seoul National University
Seoul 08826, South Korea

family, 1D hexagonal bonded tubes of sp^2 carbon possess unique electronic conductivity.[7] Nevertheless, the strong Van der Waals forces, high aspect ratio, weak dispersibility, and undetectable active centers limit the catalytic activity of CNTs. Moreover, the oxidative electrolytes and application of high current densities (≈100 mA cm^{-2}) generate strong driving forces that lead to the rapid aggregation of CNTs and modify their structure.

Diverse CNTs electrocatalysts can be prepared using various techniques such as DNA functionalization, heteroatom doping, use of a metal oxide shell (Ni, Co, or Cu) on a CNT core, and growth of atomic-scale single and bimetallic systems through organometallic complexes in combination with post-high-temperature annealing (up to ≈1200 °C).[8] The organometallic framework that binds a metal shell on carbon via ligand support represents an ideal design as it provides well-defined active centers and imparts exceptional conductivity, abundant hydrophilicity, and high catalytic performance.[9] So far, the growth of finely dispersed homogeneous heteroatom shell layers with well-defined geometry and electronic conductivity as a solution for overcoming the technological limitations of CNT-based catalysis in aqueous solutions has been challenging. According to comparative studies, the use of ligand support in heteroatom structures is not suitable for all catalytic reactions. Therefore, the catalyst design and reactant species must be studied and optimized to effectively apply this strategy. Bashyam and Zelenay suggested that oxidized cobalt and iron species in coordination with nitrogen and oxygen in functionalized carbons promote high-performance electrochemical oxygen reduction reactions (ORRs).[10] Liu and Wang developed pyrite-structured cobalt phosphosulfide on CNTs and applied it as a highly efficient HER catalyst.[11] A rational HER-catalyst design can be obtained by controlling the hybridization of CNTs with suitable heteroatoms. However, the generation of molecular oxygen limits the utility of this approach.

From the family of low-cost chalcogenides, tellurides (Te) in combination with metals, transition metal dichalcogenides (TMDs), and post-TMDs (PTMDs) have been recently applied in water electrolysis systems.[12] Compared with oxygen, sulfur, and selenium, Te has a higher metallic phase with covalency, which leads to enhanced electron conductivity and enhanced electrochemical reaction with hydronium ions (H_3O^+).[13] Consequently, Te vacancy in topological insulators is more favorable for the OER.[14] Among various Te-based electrocatalysts, $CoTe_2$, Ni_3Te_2, NiTe, $NiCoTe_4$, and $MoTe_2$ have demonstrated promising performances for the OER. [15] However, the existing Te-based catalysts cannot satisfy the strict industrial requirements for the acidic OER owing to the high overpotential (≥500 mV) at a low current density of ≈10 mA cm^{-2}.

Recently, the topological insulator Bi_2Te_3 composites have been studied extensively for electrochemical HER and OER. Pure Bi_2Te_3 is not a good electrocatalyst, however, Bi_2Te_3 with partially oxidized surfaces or Te vacancies have high HER/OER performance. Specifically, the topological surface states play a key role in enhancing catalytic performance. Topological insulators are insulating in the bulk but contain conducting surface states. The charge transfer mechanism and surface reactivity of Bi_2Te_3 can be enhanced by carbon-tailored semimetal heterostructures.[16] However, this material has not been widely applied for low-pH water electrolysis owing to its low conductivity and weak absorption of H^+ ions that limit the catalytic activity. Moreover, the effective binding energy of the reaction intermediates on the catalyst surface improves the electrocatalytic performance of Bi_2Te_3. Doping or introducing intrinsic defects without destroying the topological surface state can enhance the binding energy of the reaction intermediates and carrier mobility[17].

Considering these aspects, in this study, a well-defined oxygen-confined core–shell heterostructure composed of a Bi_2Te_3 shell was formed on a CNT (nC) core through a one-step hydrothermal process. The prepared catalysts are denoted as nC–Bi_2Te_3. The well-dispersed homogeneous growth of a post-transition metal telluride (Bi_2Te_3) with an organometallic ligand support increases the number of reactive hydroxyl functional groups on the CNT surface, thereby providing potential active sites, establishing charge injection/charge transfer intermediates, and improving the intrinsic porosity and availability of well-defined active sites for the acidic OER.

2. Results and Discussion

Figure 1 schematically illustrates the synthesis of nCBi_2Te_3 through a one-step hydrothermal process. First, Bi_2Te_3 dissolved in hexadecyltrimethylammonium bromide (CTAB) at room temperature. For the meantime, a diluted solution of CNT and cysteine (HOOC—CH—CH_2—SH)-based amino-complex-rich bovine serum albumin (BSA) protein activated at low (1–3 pH) pH. Cationic surfactant ($C_{19}H_{42}BrN$) based Bi_2Te_3 solution was gradually added to Ligand–CNT solution and kept on stirring for 12 h at room temperature (Figure 1a,b). The solution was transferred to a Teflon lined autoclave and processed at a low temperature of 120 °C for 24 h. The rapid unwinding and coiling of the protein-ligand around the CNT surface in acidic conditions prevented CNT aggregation and facilitated the shaping of the Bi_2Te_3 shell with a well-defined coaxial orientation. The process was performed at a low temperature to maximize the protein activity and ensure uniform growth of the shell layers. The binding affinity of the ligand on the CNT surface promoted the rapid dissolution and nucleation of the Bi—Te sections. Furthermore, the Bi_2Te_3: CNT ratio was maintained at 2:1 to form a large amount of Bi—Te superlattices. Several adjacent Bi—Te with Te—Te sections simultaneously formed owing to Van der Waals interactions (Figure 1c).[18] Similarly, the ratio of the ligand to the surfactant was set as 1:1 to avoid the coalescence of the Bi—Te superlattices. The large-scale preparation of nC–Bi_2Te_3 was estimated by the per-gram material yield in a 50 mL autoclave. The solution was washed, centrifuged, and dried followed by the addition of 1% carboxymethyl cellulose (CMC) binder to form thick consistent ink for deposition on nickel (Ni) foam substrate. Ni foam coated nC–Bi_2Te_3 sample dried at 120 °C for 30 min in the oven.

Figure 2a demonstrates the formation of Bi_2Te_3 cluster and its attachment on the surface of CNT (Figure 2b). CNT side Waals with Bi_2Te_3 thick cluster consisting of Bi—Te lattices were clearly seen in the TEM image (Figure 2b, inset). The FE-SEM images indicated the bamboo-type structure of nC–Bi_2Te_3 with a uniform distribution of the Bi_2Te_3 shell layers grown on CNT (Figure 1c–e). The Bi_2Te_3 shell exhibited a homogeneous distribution at the surface of the bamboo-type heterostructure, as CNT protruded from within the shell. An even rod-like heterostructure with

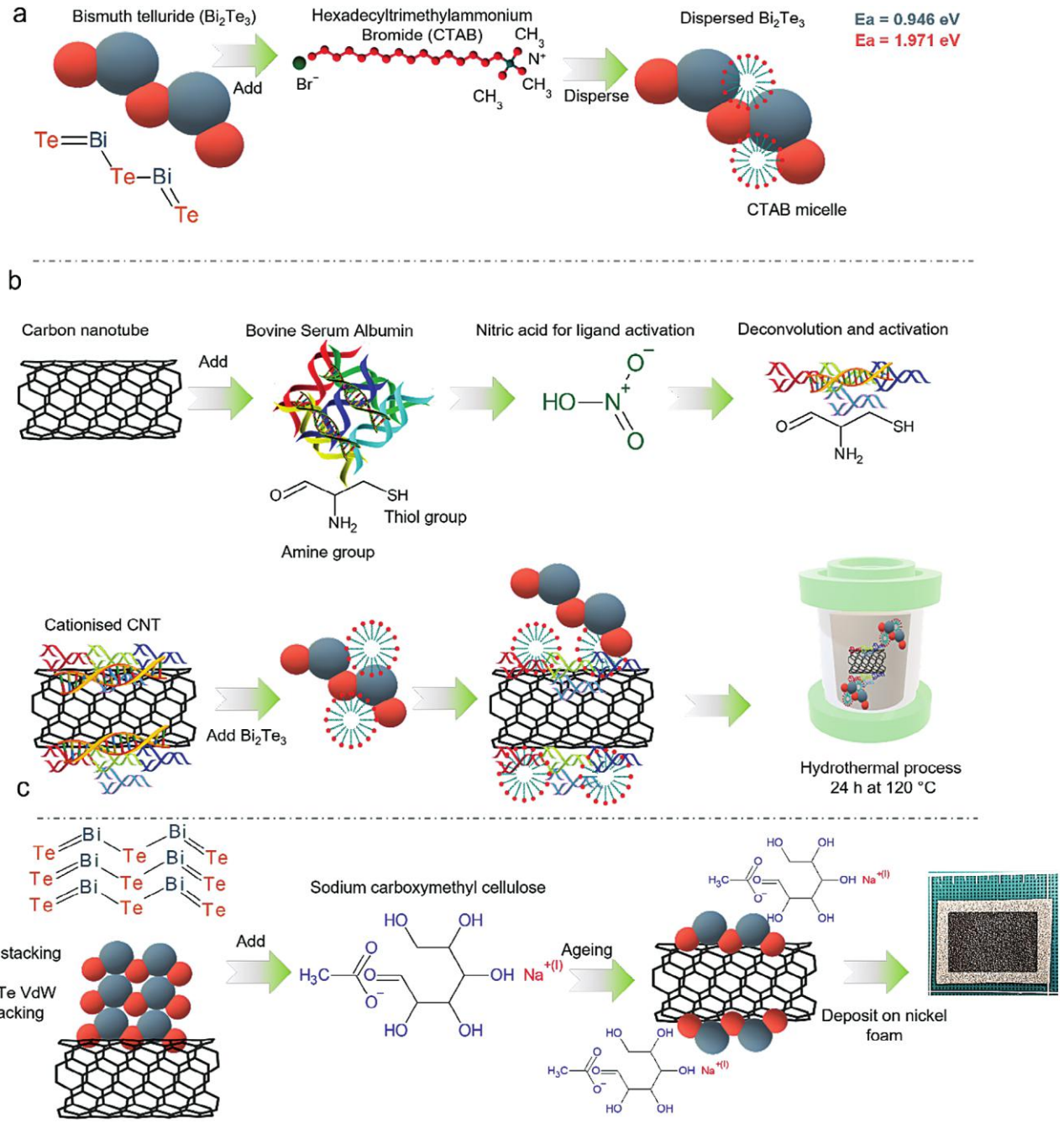

Figure 1. Schematic illustration of synthesis route of nC–Bi_2Te_3 catalyst employing a cysteine complex-based protein and surfactant complex. a) Schematic illustration depicts the chemical reaction involving Bi_2Te_3 and hexadecyltrimethylammonium bromide (CTAB), a cationic surfactant that facilitates the nucleation of Bi_2Te_3, thus forming the nC–Bi_2Te_3 catalyst. The diagram also displays the electronegativity (Ea) of Bi (0.946 eV) and Te (1.971 eV) to provide perspective. b) Schematic illustration shows the dispersion of CNT in cationised BSA, which is then adjusted to a pH of approximately 3 and followed by the addition of CTAB dissolved Bi_2Te_3. The hydrothermal reaction of carbon nanotubes and bismuth telluride with CTAB-BSA combination could yield specific nucleation sites, fostering co-axial orientation growth of the Bi_2Te_3 shell. c) Sodium carboxymethyl cellulose binder was employed to form ink and deposit nC-Bi_2Te_3 ink on Ni foam.

average diameters of 50–150 nm was observed in the TEM image which is twofold higher than pristine CNT (Figure 1f–g). XPS analyses were performed to determine the CNT, Ligand–CNT and Bi_2Te_3 composition in nC–Bi_2Te_3 (Figure 1h; Figure S2, Supporting Information). The core level C 1s spectra of nC–Bi_2Te_3 exhibited five major peaks at binding energies of 284.8, 285.6, 286, 286.5, and 287.5 eV, corresponding to the graphitic sp^2 C—C, C—O, C—N/C—OH, C═O and O—C═O bonds, respectively. The peak related to the sp^2 C—C bonds exhibited a slight positive shift of ≈0.3 eV, attributable to the doping of Bi_2Te_3 on the CNT

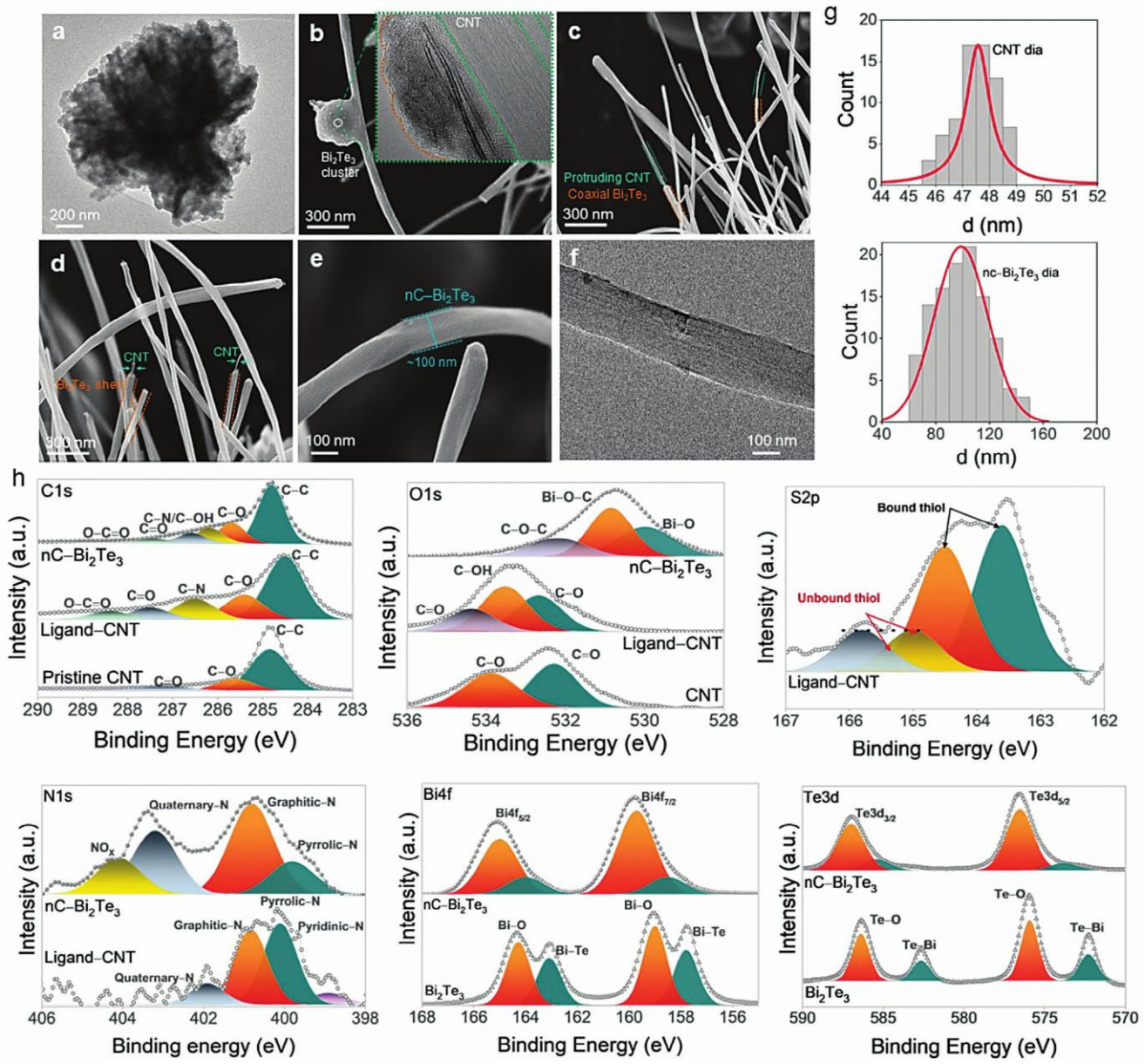

Figure 2. Morphology, and chemical composition of nC–Bi_2Te_3. a) TEM image of Bi_2Te_3 cluster formed during the growth process. b) FE-SEM images of the nC–Bi_2Te_3 catalyst. Cluster consists of Bi—Te superlattices coaxially grown on CNT (inset TEM image). c–f) Bamboo-like core–shell structure of nC–Bi_2Te_3 catalyst shown in FE-SEM images. g) Frequency distribution graph of the diameter of the CNT and nC–Bi_2Te_3 catalyst. h) High-resolution C1s and O1s XPS spectra of CNT, Ligand–CNT, and nC–Bi_2Te_3 catalyst, Bi4f and Te3d XPS spectra of Bi_2Te_3 and nC–Bi_2Te_3, N1s spectra of ligand–CNT and nC–Bi_2Te_3 samples, S2p spectra of Ligand–CNT.

because the shell layers did not destroy the sp^2 carbon bonding. The three deconvoluted peaks at 530, 531, and 532 eV in the high-resolution O 1s spectra indicate the presence of Bi—O, Bi—O—C and C—O—C bonds, respectively. Bi—O—C chemical bond formation between conductive CNT and Bi_2Te_3 shell able to promote catalyst activation with fast charge transfer and OER stability. The two strong peaks located at 159.7 and 165.15 eV were attributable to Bi $4f_{7/2}$ and Bi $4f_{5/2}$, respectively demonstrating the characteristics Bi—O chemical bond. While Bi—Te displayed at lower binding energies of 158.5 and 164 eV in Bi 4f spectrum. These peaks exhibited a positive shift of ≈1 eV toward high B.E. Additionally, the peaks for Te $3d_{5/2}$ and Te $3d_{3/2}$ exhibited higher binding energies at 576.5 and 587 eV, attributed to Te—O chemical bonds, respectively. Te $3d_{5/2}$ and Te $3d_{3/2}$ possess higher binding energy with of ≈1 and 0.7 eV than Bi_2Te_3. The XPS results indicated the higher oxidation state of Bi—O and Te—O in heterostructure leading to enhanced intrinsic OER activity. In other words, the BSA ligand promoted the formation of —OH in between shell and CNT. The N 1s spectra of Ligand–CNT showed peaks associated with pyrrolic-*N* and quaternary-type amines with binding energies of 398.9 and 405 eV, respectively. Interestingly, the N 1s spectra of nC–Bi_2Te_3

exhibited pyrrolic–N (400 eV), graphitic–N (401 eV), quaternary-type amines (403 eV) and oxidized–N (404 eV). Higher amounts of pyrrolic and graphitic —N improves the conductivity of the structure and increase charge storage behavior. Bound thiol group —SH was observed in Ligand–CNT S2p XPS at binding energies of ≈163.5 and ≈164.5 eV, providing evidence that the thiol group in ligand helps to promote the growth of core–shell structure. The surface composition exhibited that the CNT was covered with a highly oxidative ligand-supported Bi_2Te_3, which indicated the high OER functionality of the as-prepared catalyst. The results of the XPS elemental studies of nC–Bi_2Te_3 and Bi_2Te_3 in terms of survey and narrow analyses are presented in Table S1 (Supporting Information).

HR-TEM was performed to characterize the superstructure of the catalyst assembled from the rhombohedral-type Bi_2Te_3 shell and fully supported on the CNT with an average diameter of 80–150 nm (**Figure 3**a). The focused TEM images showed a pair of Bi—Te superlattices formed at the CNT side walls, where charge interference dominantly occurs (Figure 3b). In the superlattices, the distance between the Bi—Te sections was 2 nm, like that in the bulk Bi_2Te_3 cluster formed during the growth process. Consecutive pairs of superlattices were assembled on the CNT. Self-assembling progressive pairs of 2, 4, and 6 nm of single, bi-, and tri-layers of Bi—Te superlattices were built on the CNT, respectively. The pairs were aligned through weak Van der Waals forces. Superlattices grew parallel to the axis of the CNT with angular and parallel orientations. A clear Bi—Te lattice intact in the shell layer demonstrated that topological charges on the surface of Bi_2Te_3 take part in the charge transfer mechanism of the catalyst. The high-angle annular dark-field (HAADF) TEM image and corresponding elemental mapping profile indicated the even distribution of Bi and Te elements on the side walls of the CNT, with C and O elements distributed on the overall surface (Figure 3c). The EDX spectra indicated the contents of C (89.80%), O (1.65%), Bi (5.95%), and Te (2.60%) elements in nC–Bi_2Te_3. TEM EDS analysis was performed at different sites of TEM mesh deposited with catalyst (Figure S3 and Table S2, Supporting Information). The nanocrystal-coated CNT assembly prevented the oxidation and aggregation of the catalyst at low pH. The corresponding FFT image indicated that the Bi—Te layered system had a crystalline structure with the layer spacings of 0.3 (3 Å) and 0.24 (2.4 Å) nm associated with the (015) and (1010) crystallographic planes of the rhombohedral Bi_2Te_3 phase, respectively (Figure 3e). The crystal index of graphitic carbon with a d-spacing of 0.33 nm (3.3 Å) was also observed. The crystal structure of nC—Bi_2Te_3 was confirmed from the XRD results (Figure 3f). Specifically, nC–Bi_2Te_3 exhibited characteristic diffraction peaks at 17.30°, 27.8°, and 38°, indexed to the (006), (015), and (1010) facets of a rhombohedral Bi_2Te_3 phase (JCPDS no. 15–0863), respectively. After heterostructure formation, the dominant graphitic carbon peak at 26.02° (JCPDS no. 75–1621), indexed to 002, decreased in magnitude, indicating surface reconstruction and vacancy formation in the carbon lattice. ^{17}O—NMR studies of the CNT and nC–Bi_2Te_3 heterostructure were performed. The results indicated that nC–Bi_2Te_3 synthesized at a low hydrothermal temperature range of ≈120 °C increased the number of surfaces —OH hydroxyl groups. The same observations were made for the CNT structure, and no distinct peak of the —OH group was observed. The surface of Bi_2Te_3 coated on CNT was prone to oxidation in the presence of the BSA protein and cetrimonium bromide surfactant, resulting in the enhanced catalytic activity for acidic OER (Figure 3g). Raman spectroscopy was performed to investigate the surface defects of the nC–Bi_2Te_3 heterostructure. As shown in Figure 2h, nC–Bi_2Te_3 exhibited two peaks at 660 and 750 cm^{-1}, attributable to the Raman modes of A_{1g}^1 and E_g^2 associated with the stretching modes of Bi—Te and Te—Te shown in Figure 3h, inset respectively.[19] The higher D peak at (1343 cm^{-1}) with higher (I_D/I_G = 0.7) ratio of nC–Bi_2Te_3 than that of CNT (I_D/I_G = 0.10) and Ligand–CNT (I_D/I_G = 0.6) indicated the formation of surface defects on CNT occur during attachment of BSA ligand and subsequently increased during hydrothermal growth of surface shell layers.

The electrocatalytic OER performance of the nC–Bi_2Te_3 catalyst was evaluated in 0.5 M H_2SO_4 and compared with those of commercial Ni foam, Bi_2Te_3, CNT, and ligand–CNT catalysts. As shown in **Figure 4**a, nC–Bi_2Te_3 required an extremely small overpotential of 160 and 380 mV to achieve a current density of 10 and 100 mA cm^{-2}, respectively thereby outperforming commercial Bi_2Te_3 (820 mV), CNT (480 mV), and Ligand–CNT (470 mV) electrocatalysts, which demonstrated its potential as an outstanding OER catalyst (Tables S3–S4, Supporting Information). The Tafel slope of the core–shell nC–Bi_2Te_3 heterostructure was 30 mV dec^{-1} (Figure 4b), considerably smaller than that of Bi_2Te_3 (208 mV dec^{-1}), CNT (150 mV dec^{-1}), Ligand–CNT (93 mV dec^{-1}), and Ni foam (220 mV dec^{-1}). In other words, the proposed heterostructure exhibited optimal catalytic kinetics, leading to superior OER performance. The electrochemical active surface area (ECSA) of the catalysts was determined by calculating the double layer capacitance (C_{dl}) and specific capacitance (C_S) to estimate the active catalytic surface. The C_{dl} of nC–Bi_2Te_3 (3 mF cm^{-2}) was higher than those of Ligand–CNT (2.8 mF cm^{-2}), CNT (2 mF cm^{-2}), Bi_2Te_3 (0.45 mF cm^{-2}), and Ni foam (0.3 mF cm^{-2}), with the corresponding ECSA values being 75, 70 50, 11.25, and 7.5 cm^2, respectively. This finding indicated that the Bi_2Te_3 coating on CNT triggered the exposure of active sites of catalyst, which simultaneously enhanced the electronic conductivity and surface area of nC–Bi_2Te_3 for acidic OER (Figure 4c). Electrochemical impedance spectroscopy (EIS) analyses were performed to confirm the faster OER kinetics and higher charge mobility of nC–Bi_2Te_3 compared with those of CNT, Ligand–CNT and Bi_2Te_3. Randles-type circuit used to calculate charge transfer resistance (R_{ct}) of electrodes (Figure 4g). Owing to its smallest sheet resistance (R_s), nC–Bi_2Te_3 exhibited an R_{CT} of 1.5 Ω, considerably lower than those of CNT (23 Ω), Ligand–CNT (15.3 Ω), Bi_2Te_3 (34.8 Ω), and Ni foam (30 Ω). This low value and enhanced electrical conductivity indicated that shell formation of Bi_2Te_3 on CNT increased the number of defect-rich sites and charge mobility on the catalyst surface (Figure 4h). The electrode contact of nC–Bi_2Te_3 was noted to be improved, in terms of R_s (0.35 Ω), compared with those of Ni, Bi_2Te_3, CNT, and Ligand–CNT. **Table 1** lists the electrochemical parameters.

The electrocatalytic OER performance of nC–Bi_2Te_3 catalyst was further examined in 1 M KOH and compared with those of commercial Ni foam, Bi_2Te_3, CNT, and Ligand–CNT catalysts. As shown in Figure 4d, nC–Bi_2Te_3 required an overpotential of 110, 540, and 730 mV to achieve a current density of 10, 100, and 200 mA cm^{-2}, respectively thereby outperforming Bi_2Te_3 (470 mV), CNT (510 mV), and Ligand–CNT (430 mV)

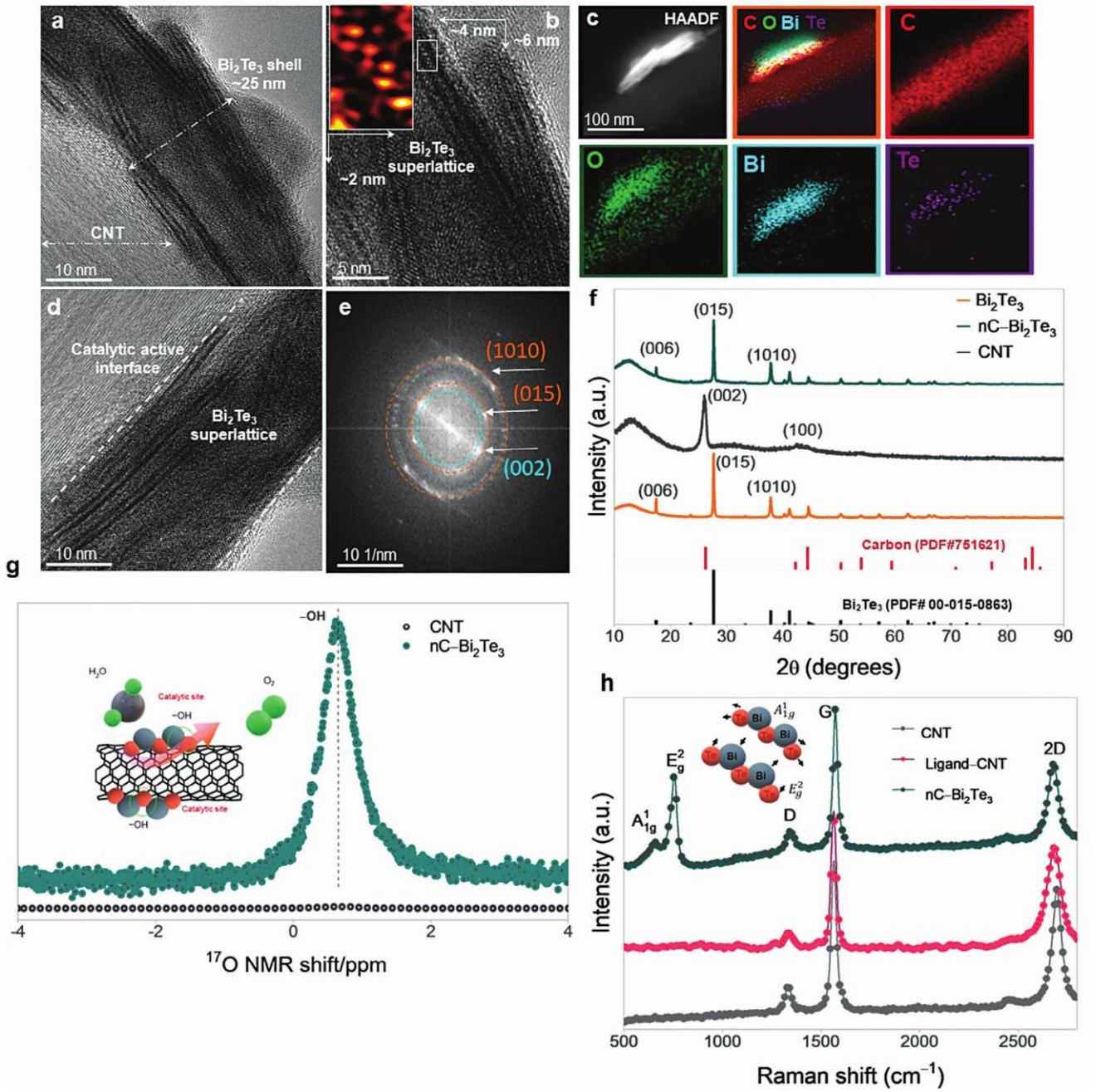

Figure 3. a,b) HRTEM images of nC–Bi_2Te_3 showing Bi_2Te_3 deposited on the CNT surface. The corresponding inset image shows Bi—Te lattice. c) HAADF TEM image and energy dispersive X-ray (EDX) elemental mapping images. d) HRTEM image of nCBi_2Te_3 showed Interface between the Bi_2Te_3 cluster and CNT side walls. e) Corresponding FFT showing the orientation alignment of CNT (002) and crystalline Bi_2Te_3 with (015) and (1010) crystal planes. f) XRD patterns of the as prepared nC–Bi_2Te_3 heterostructure along with CNT and Bi_2Te_3 powder. g) ^{17}O NMR of CNT and nC–Bi_2Te_3 samples recorded with NMR at 600 MHz. Identification of real active sites with ^{17}O NMR for predicting the OER activity (inset). h) Raman spectrum of CNT, ligand-CNT and nC–Bi_2Te_3 at 600 cm^{-1} to 2700 cm^{-1}. Illustration of stretching modes of bismuth telluride on CNT surface (inset).

electrocatalysts. The Tafel slope of the nC–Bi_2Te_3 heterostructure was 23 mV dec^{-1} (Figure 4e), considerably smaller than that of Ni foam (72 mV dec^{-1}), Bi_2Te_3 (46 mV dec^{-1}), CNT (38 mV dec^{-1}), and Ligand–CNT (25 mV dec^{-1}). The C_{dl} of nC–Bi_2Te_3 (3.6 mF cm^{-2}) was higher than those of Ni foam (0.4 mF cm^{-2}), Bi_2Te_3 (0.90 mF cm^{-2}), CNT (0.91 mF cm^{-2}), and Ligand–CNT (0.95mF cm^2) with the corresponding ECSA values of 90, 10, 22.5, 22.7, and 23.75 mF cm^2, respectively (Figure 4f). Electrochemical impedance spectroscopy (EIS) analyses were performed to confirm the faster OER kinetics and higher charge mobility of nC—Bi_2Te_3 compared with those of Ni foam, Bi_2Te_3, CNT, and Ligand–CNT. Due to the smallest sheet resistance (R_S = 0.66), nC–Bi_2Te_3 exhibited an R_{ct} of 6.12 Ω, considerably lower than those of Ni foam (158 Ω), Bi_2Te_3 (128 Ω),

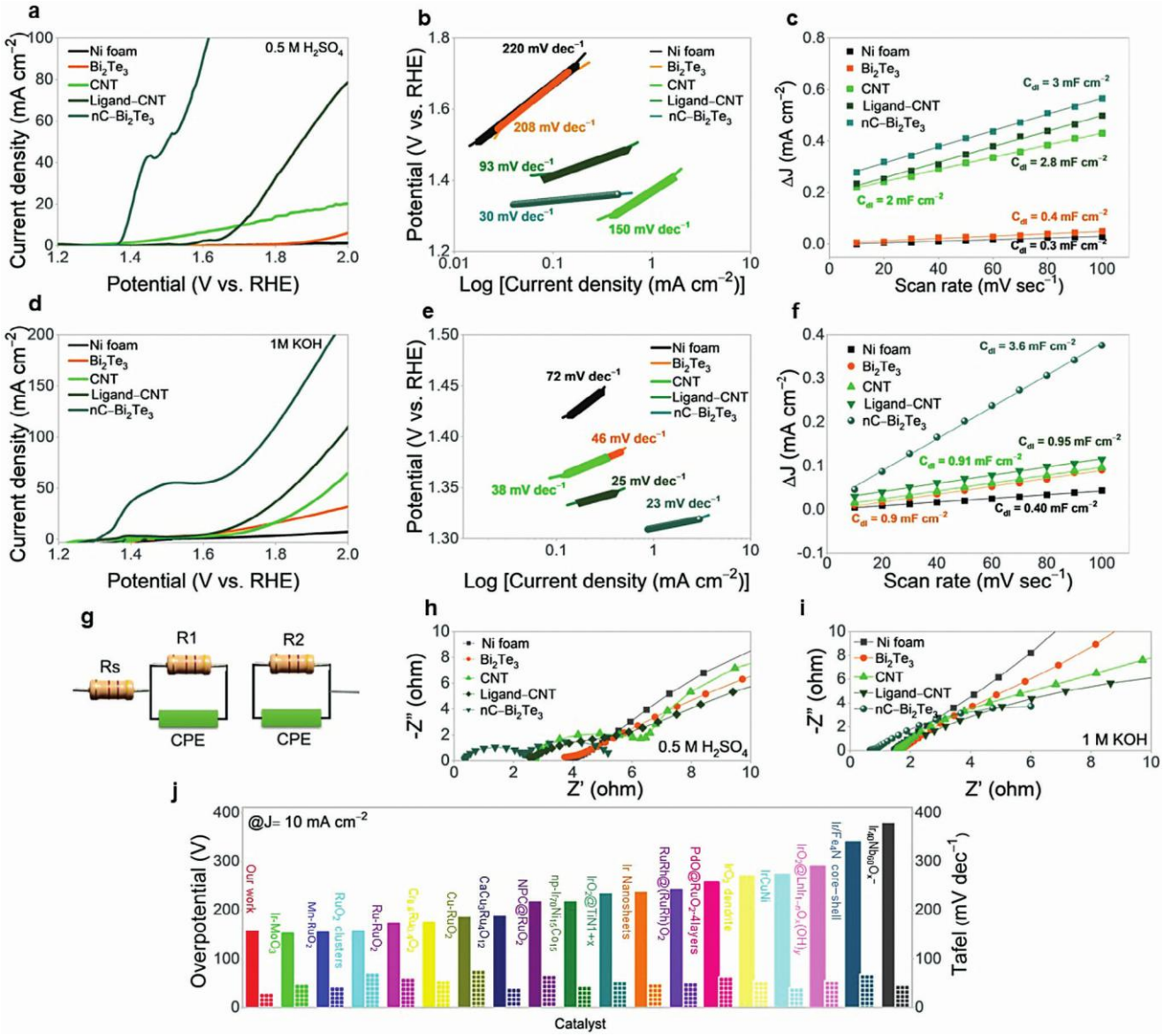

Figure 4. a–c) LSV, corresponding Tafel curves, and capacitive current (C_{dl}) at 0.26 V vs RHE as a function of the scan rate for Nickel, Bi_2Te_3, CNT, Ligand–CNT and nC–Bi_2Te_3 catalysts in 0.5 M H_2SO_4 at 5 mV s^{-1}. d–f) LSV, corresponding Tafel curves and capacitive current (C_{dl}) at1.10 V vs RHE as a function of the scan rate for Nickel, Bi_2Te_3, CNT, Ligand–CNT and nC–Bi_2Te_3 catalyst in 1M KOH at 5 mV s^{-1}. g) Randles type circuit for EIS fitting of Nyquist plots of corresponding catalysts for measurement of the sheet resistance (RS) and charge transfer resistance (R_{CT}). h,i) Nyquist plots of corresponding catalysts in acid and alkaline electrolyte. j) Comparison of overpotential and Tafel of state of art precious metal catalyst with nC–Bi_2Te_3 catalyst in acid electrolyte.

Table 1. Electrochemical performance of different OER catalysts in 0.5 M H_2SO_4 electrolyte.

Parameters	Overpotential and corrosion			Surface area		Impedance
OER catalyst	η10 [mV]	Tafel [mV dec^{-1}]	ECSA [cm^2]	C_{dl} [mF cm^{-2}]	R_s [Ω]	R_{CT} [Ω]
Ni Foam	–	220	7.5	0.32	3.8	30
Bi_2Te_3	820	208	11.5	0.45	3.8	34.8
CNT	480	150	50	2	2.7	23
Ligand–CNT	470	93	70	2.8	2.5	15.3
nC–Bi_2Te_3	160	30	75	3	0.35	1.5

Table 2. Electrochemical performance of different OER catalysts in 1 M KOH electrolyte.

Parameters	Overpotential and corrosion			Surface area		Impedance
OER catalyst	η10 [mV]	Tafel [mV dec^{-1}]	ECSA [cm^2]	C_{dl} [mF cm^{-2}]	R_s [Ω]	R_{CT} [Ω]
Ni Foam	–	72	10	0.4	1.45	158
Bi_2Te_3	470	46	22.5	0.9	2.05	128
CNT	510	38	22.7	0.91	1.54	25
Ligand–CNT	430	25	23.75	0.95	1.5	23
nC–Bi_2Te_3	110	23	90	3.6	0.66	6.12

CNT (25 Ω), and Ligand–CNT (23 Ω), respectively (Figure 4i). The improved electrical contact and lower R_{ct} demonstrated swift electron transfer mechanism on nC–Bi_2Te_3 catalyst. **Table 2** lists the electrochemical parameters of the catalyst in 1 M KOH electrolyte. The overpotential and Tafel slopes were smaller than or comparable to those of recently reported precious metal structures based on Ru and Ir metals (Figure 4j).[20]

The low acidic OER stability is a well-known bottleneck in industrial water splitting and fuel cell technologies. Long-term chronoamperometric analyses were performed for 22 h using 0.5 M H_2SO_4. The nC–Bi_2Te_3 exhibited a current density of 10 ± 1 mA cm^{-2} and high stability over 22 h at constant potential of 1.39 V versus RHE (**Figure 5**a). The sequential high-speed optical images of nC–Bi_2Te_3 heterostructure electrode helped visualize the abundance of O_2 bubbles formed during the OER test (Figure 5a, inset). Figure 5b shows the cross-sectional FE-SEM images of nC–Bi_2Te_3 heterostructure coated on nickel foam showed undamaged layer structure after a long term chronoamperometric stability test. Slight aggregation of Bi_2Te_3 shell on CNT was observed after in high-resolution FE−SEM image. Post-stability XRD and XPS analyses were made to examine changes in catalyst composition (Figure 5c). Post stability nC–Bi_2Te_3 sample exhibited characteristic diffraction peaks at 27.8°, and 38°, indexed to the (015), and (1010) facets of a rhombohedral Bi_2Te_3 phase (JCPDS no. 15–0863), respectively, while sharp Ni peaks originated from based substrate. No shift in XRD peaks were observed. To monitor the surface and chemical state changes, XPS results Post OER and as-synthesized results of nC–Bi_2Te_3 were examined. Post OER C1s deconvoluted to four peaks with higher binding energies at 284.7, 285.5, 286.4, and 287.5 eV, assigned to C—C, C—O, C—N/C—OH and —OH respectively. N1s spectra showed peaks at 400.3 eV, 401.2 eV, 403.1, and 404 attributed to Pyrrolic–N, graphitic–N, amines and —NO_x, respectively. Higher oxidation state of amines provides evidence N species in heterostructure help to promote OER mechanisms. However, a positive shift of ≈3 eV is observed in O1s, due to the oxidation reaction mechanism. O1s spectra of Post OER showed a positive shift of ≈3 eV with higher binding energies of 532.1, 533, 534, and 535 eV assigned to the oxidation state of Bi—Te, Bi—O—C, —OH and absorbed water molecules at the catalyst surface. Bi4f$_{7/2}$, Bi4f$_{5/2}$, Te3d$_{5/2}$, and Te3d$_{3/2}$ show the slight positive shift of ≈0.1–0.5 eV owing to the oxidation state electrolyte on the catalyst surface. The stabilized C—C sp^2 remains unchanged while the formation of active Bi—O—C demonstrated the origin of catalyst activation. The inherent structure and composition of the OER catalyst were maintained after the long-term stability test, which demonstrated that the catalyst could withstand harsh acidic conditions.

3. Conclusion

This work provides novel insights into nanomaterial design with a non-precious post-transition-metal-carbon structure that facilitates the achievement of extremely low overpotential for acidic OERs. The proposed organometallic framework successfully tuned the oxygen in metal tellurides, thereby exhibiting an overpotential of only 160 mV at 10 mA cm^{-2} in 0.5 M H_2SO_4. The substitution of conventional TMDs with PTMDs could help clarify the unusual OER activity of the catalytic system. Overall, nC–Bi_2Te_3 is an effective catalyst that can promote the scaled-up commercialization of efficient PEMWE systems.

4. Experimental Section

Synthesis of nC–Bi_2Te_3 Catalyst: First, 0.5 g of CNT was dispersed in a cysteine-based protein dispersion. Next, 3 mg mL^{-1} protein was completely dissolved, and a low pH (≈1) was maintained by adding nitric acid. Bi_2Te_3 was dispersed in the surfactant and mixed with the CNT–protein complex. The solution was transferred to a 50 mL autoclave and heated in a vacuum oven at 90 °C for 1 h to initiate the activation of the cysteine complex. Next, the mixture was heated to 120 °C for 24 h in a vacuum oven. The solution was centrifuged (Tabletop centrifuge, Cef-8, Daihan Scientific, South Korea) at 3000 RPM and dried in an oven at 100 °C to obtain the nC–Bi_2Te_3 powder. A 1% carboxymethyl cellulose binder was added to the powder that was ground in an agate mortar. The ink was deposited onto the nickel foam, air-dried, and heated in an oven at 200 °C for 1 h. The performance of five catalysts for OER: commercial Ni foam, Bi_2Te_3, CNT, Ligand–CNT and nC–Bi_2Te_3 catalysts were compared.

Morphological and Structural Characterization: The surface morphology was studied through field-emission scanning electron microscopy (FE-SEM; Carl Zeiss SIGMA, Germany). A JEOL-JEM F200, Japan field-emission transmission electron microscope was used for acquiring high-resolution transmission electron microscopy (HR-TEM) images and electron dispersive X-ray spectroscopy (EDX) spectra. The nC–Bi_2Te_3 sample was dissolved in deionized water and dropped cast on lacey formvar/carbon on a 300-mesh Cu substrate for TEM. The grids were dried overnight before TEM. An X-ray photoelectron spectroscopy (XPS) system (Thermo Fisher Scientific (*K*-Alpha+)), USA was used for surface elemental identification and quantification. Moreover, a micro-Raman spectrometer (FEX), NOST, South Korea was used for Raman spectroscopy, involving an excitation laser wavelength of 531 nm, an excitation laser power of 0.3 mW, and a spectral resolution of 1.9–2.1 cm^{-1}. X-ray diffraction analysis was performed using a Bruker-AXS, New D8-advance device, USA. ^{17}O nuclear magnetic resonance (NMR) analysis examined at Nuclear Magnetic Resonance Spectrometer-600 MHz, VNS, Varian, USA.

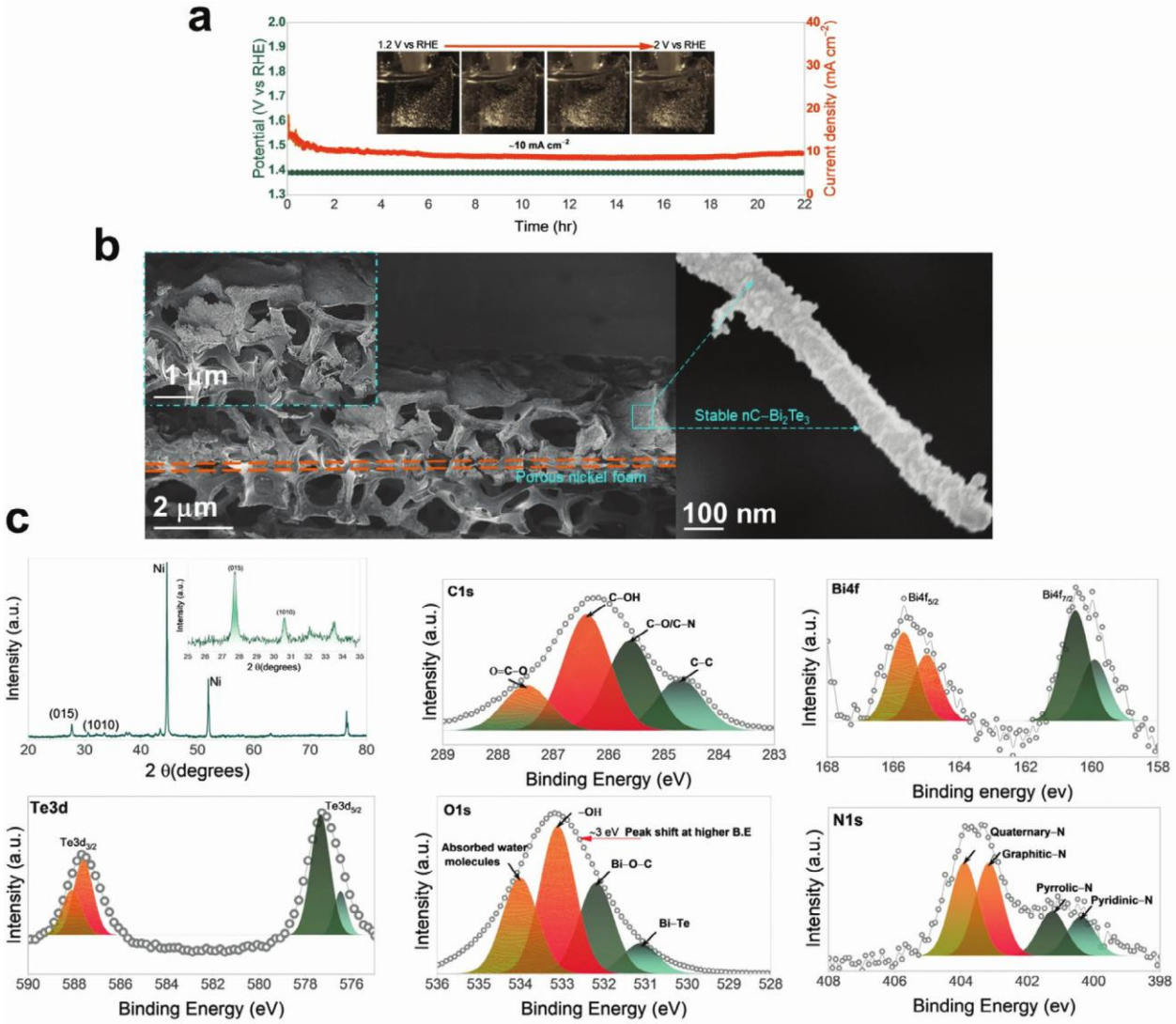

Figure 5. Electrochemical long-term stability of nC–Bi_2Te_3 catalyst. a) Chronoamperometric measurements of nC–Bi_2Te_3 heterostructure at 1.39 V versus. RHE for 22 h, Sequential high-speed optical images of nC–Bi_2Te_3 heterostructure from 1.2 V versus. RHE to 2 V versus. RHE (Inset). b) Cross-sectional FE-SEM images of nC–Bi_2Te_3 heterostructure coated Ni foam after long-term stability testing. c) XRD and XPS analysis of nC–Bi_2Te_3 catalyst after long-term stability test.

Electrochemical Measurements: All electrochemical measurements such as linear sweep voltammetry (LSV), cyclic voltammetry (CV), chronoamperometry, and R_{CT} measurements were performed using a Potentiostat SP-300 system, USA. All samples were tested in a 0.5 M H_2SO_4 and 1 M KOH electrolyte solution at room temperature (≈25 °C). Three-electrode cell systems were used and equipped with Ag/AgCl (saturated KCl) as the reference electrode and Pt wire as the counter electrode. nC–Bi_2Te_3 ink was deposited on nickel foam electrode, cut to form samples sized 1.5 × 1.5 cm^2, and used as a working electrode for OER measurement (Figure S4, Supporting Information). Before measurement, each sample was polarized for 1000 cycles to obtain a stable scan. For the OER, anodic LSV tests were performed at 1.2–2 V versus RHE at a scan rate of 5 mV s^{-1}. The OER overpotential in the was calculated as:

$$E \text{ versus RHE} = E \text{ versus Ag/AgCl} + 0.197\text{V} + 0.059 \times \text{pH} \quad (1)$$

$$\eta = E \text{ versus RHE} - 1.23 \quad (2)$$

The reference electrode voltage (E versus Ag/AgCl) was converted to the reversible hydrogen electrode voltage (E versus RHE). The potential of the Ag/AgCl reference electrode was 0.197 V. Tafel slopes were calculated from the LSV curves according to the following equation: $n = a + b \log j$, where a and b are constants, and j is the current density. Notably, this equation clarifies the mechanism for the kinetic reaction during the OER. Chronoamperometry tests were performed to analyze the long-term stability of nC–Bi_2Te_3 at acidic pH. A current density of 10 ± 1 mA cm^{-2} was recorded for 22 h at an applied voltage of 1.39 V versus RHE. The C_{dl} of the electrodes was calculated by plotting the capacitance current against the scan rate of 10–100 mV s^{-1} (Figure S5, Supporting Information).

Supporting Information

Supporting Information is available from the Wiley Online Library or from the author.

Acknowledgements

This work was supported by the National Research Foundation of Korea (NRF) grant funded by the Korea government (MSIT) (No. 2021R1C1C1012119), the Industrial Technology Innovation Program (No. 20007058, Development of safe and comfortable human augmentation hybrid robot suit) funded by the Ministry of Trade, Industry & Energy (MOTIE, Korea), and the Chung-Ang University Graduate Research Scholarship in 2022.

Conflict of Interest

The authors declare no conflict of interest.

Data Availability Statement

The data that support the findings of this study are available from the corresponding author upon reasonable request.

Keywords

bismuth telluride, carbon nanotubes, electrocatalysts, heterostructures, organic synthesis, oxygen evolution reaction

Received: August 18, 2023
Revised: October 19, 2023
Published online: November 9, 2023

[1] a) S. Chu, A. Majumdar, *Nature* **2012**, *488*, 294; b) Y. Jiao, Y. Zheng, M. Jaroniec, S. Z. Qiao, *Chem. Soc. Rev.* **2015**, *44*, 2060; c) J. Saha, S. Verma, R. Ball, C. Subramaniam, R. J. S. Murugavel, *Small* **2020**, *16*, 1903334; d) K. Zhang, R. Zou, *Small* **2021**, *17*, 2100129;

[2] a) Y. Chen, C. Liu, J. Xu, C. Xia, P. Wang, B. Y. Xia, Y. Yan, X. Wang, *Small Struct.* **2022**, *4*, 2200130; b) J. Zhao, Y. He, J. Wang, J. Zhang, L. Qiu, Y. Chen, C. Zhong, X. Han, Y. Deng, W. Hu, *Chem. Eng. J.* **2022**, *435*, 134261; c) M. Kim, J. Kim, L. Qin, S. Mathew, Y. Han, O. L. Li, *Prog. Nat. Sci.: Mater. Int.* **2022**, *32*, 608; d) Y. Zhang, X. Teng, Z. Ma, R. Wang, W.-M. Lau, A. Shan, *Prog. Nat. Sci.: Mater. Int.* **2022**, *32*, 554.

[3] Y. Wang, B. Kong, D. Zhao, H. Wang, C. Selomulya, *Nano Today* **2017**, *15*, 26.

[4] a) S. Park, Y. Shao, J. Liu, Y. Wang, *Energy Environ. Sci.* **2012**, *5*, 9331; b) E. J. A. C. Antolini, *ACS Catal.* **2014**, *4*, 1426; c) H. Chen, J. Liu, X. Wu, C. Ye, J. Zhang, J. L. Luo, X. Z. J. S. Fu, *Small* **2022**, *18*, 2204100; d) H. Liu, Z. Zhang, M. Li, Z. Wang, X. Zhang, T. Li, Y. Li, S. Tian, Y. Kuang, X. J. S. Sun, *Small* **2022**, *18*, 2202513; e) K. Huang, C. Lin, G. Yu, P. Du, X. Xie, X. He, Z. Zheng, N. Sun, H. Tang, X. Li, M. Lei, H. Wu, *Adv. Funct. Mater.* **2023**, *33*, 2211102.

[5] a) R. Frydendal, E. A. Paoli, B. P. Knudsen, B. Wickman, P. Malacrida, I. E. L. Stephens, I. Chorkendorff, *ChemElectroChem* **2014**, *1*, 2075; b) C. Spöri, J. T. H. Kwan, A. Bonakdarpour, D. P. Wilkinson, P. Strasser, *Angew. Chem.* **2017**, *56*, 5994.

[6] a) D. Das, S. Santra, K. K. Nanda, K. K. J. A. Nanda, *ACS Appl Mater Interfaces* **2018**, *10*, 35025; b) M. Zhang, J. Chen, H. Li, P. Cai, Y. Li, Z. Wen, *Nano Energy* **2019**, *61*, 576; c) H. Li, S. M. Xu, H. Yan, L. Yang, S. J. S. Xu, *Small* **2018**, *14*, 1800367; d) G.-L. Tian, M.-Q. Zhao, D. Yu, X.-Y. Kong, J.-Q. Huang, Q. Zhang, F. Wei, *Small* **2014**, *10*, 2251; e) Y. Li, B. Jia, Y. Fan, K. Zhu, G. Li, C.-Y. Su, *Adv. Energy Mater.* **2018**, *8*, 1702048.

[7] a) S. Iijima, C. Brabec, A. Maiti, J. J. T. J. o. c. p. Bernholc, *J. Chem. Phys.* **1996**, *104*, 2089; b) S. Iijima, T. Ichihashi, *Nature* **1993**, *363*, 603; c) L.-C. Qin, X. Zhao, K. Hirahara, Y. Miyamoto, Y. Ando, S. Iijima, *Nature* **2000**, *408*, 50.

[8] a) A. A. Arbab, A. A. Memon, I. A. Sahito, N. Mengal, K. C. Sun, M. Ali, S. H. Jeong, *J Mater Chem* **2018**, *6*, 8307; b) X. Liu, M. Park, M. G. Kim, S. Gupta, X. Wang, G. Wu, J. Cho, *Nano Energy* **2016**, *20*, 315; c) Y. Chen, C. Tian, T. Jiang, C. Maheu, J. P. Hofmann, L. Molina-Luna, R. Riedel, Z. J. C. Yu, *ChemPlusChem* **2022**, *87*, 202200338; d) L. Zhang, Q. Wang, R. Si, Z. Song, X. Lin, M. N. Banis, K. Adair, J. Li, K. Doyle-Davis, R. J. S. Li, *Small* **2021**, *17*, 2004453; e) S. H. Ahn, A. Manthiram, *Small* **2020**, *16*, 2002511.

[9] a) A. A. Arbab, K. C. Sun, I. A. Sahito, M. B. Qadir, S. H. Jeong, *Appl. Surf. Sci.* **2015**, *349*, 174; b) A. A. Arbab, K. C. Sun, I. A. Sahito, M. B. Qadir, Y. S. Choi, S. H. Jeong, *ACS Appl Mater Interfaces* **2016**, *8*, 7471.

[10] R. Bashyam, P. Zelenay, *Nature* **2006**, *443*, 63.

[11] W. Liu, E. Hu, H. Jiang, Y. Xiang, Z. Weng, M. Li, Q. Fan, X. Yu, E. I. Altman, H. Wang, *Nat. Commun.* **2016**, *7*, 10771.

[12] a) J. Su, T. Minegishi, Y. Kageshima, H. Kobayashi, T. Hisatomi, T. Higashi, M. Katayama, K. Domen, *J. Phys. Chem. Lett.* **2017**, *8*, 5712; b) B. Wang, X. Wang, P. Wang, A. Kuang, T. Zhou, H. Yuan, H. Chen, *Appl. Surf. Sci.* **2021**, *544*, 148842; c) L. Zhao, G. Yu, M. Lv, X. Huang, H. Zhu, W. Chen, *J. Colloid Interface Sci.* **2023**, *629*, 971.

[13] a) Z. Chen, M. Chen, X. Yan, H. Jia, B. Fei, Y. Ha, H. Qing, H. Yang, M. Liu, R. Wu, *ACS Nano* **2020**, *14*, 6968; b) X. Wang, Z. Mao, X. Mao, X. Hu, F. Gao, M. Gao, Q.-L. Wu, X. Lyu, A. Du, X. Xu, Y. Jia, L. Wang, *Adv. Sci.* **2023**,*10*, 2206204.

[14] a) J. Xu, Z. Lian, B. Wei, Y. Li, O. Bondarchuk, N. Zhang, Z. Yu, A. Araujo, I. Amorim, Z. Wang, B. Li, L. Liu, *ACS Catal.* **2020**, *10*, 3571; b) Z. Jin, H. Zheng, Y. Dong, S. Guo, X. Li, X. Kang, M. Xia, J. Wang, Z. Li, T. Jiao, *ACS Sustainable Chem. Eng.* **2022**, *10*, 15166.

[15] a) Q. Gao, C.-Q. Huang, Y.-M. Ju, M.-R. Gao, J.-W. Liu, D. An, C.-H. Cui, Y.-R. Zheng, W.-X. Li, S.-H. Yu, *Angew. Chem.* **2017**, *56*, 7769; b) L. Yang, H. Qin, Z. Dong, T. Wang, G. Wang, L. J. S. Jiao, *Small* **2021**, *17*, 2102027; c) Y. Li, M. Wang, Y. Yi, C. Lu, S. Dou, J. J. S. Sun, *Small* **2021**, *17*, 2005573; d) C. Gao, D. Rao, H. Yang, S. Yang, J. Ye, S. Yang, C. Zhang, X. Zhou, T. Jing, X. Yan, *New J. Chem.* **2021**, *45*, 5589; e) H. Li, C. Li, B. Tao, S. Gu, Y. Xie, H. Wu, G. Zhang, G. Wang, W. Zhang, H. Chang, *Adv. Funct. Mater.* **2021**, *31*, 2010901; f) T. Li, Y. Deng, X. Rong, C. He, M. Zhou, Y. Tang, H. Zhou, C. Cheng, C. J. S. Zhao, *SmartMat* **2023**, *4*, e1142.

[16] a) K. Yin, Z. Cui, X. Zheng, X. Yang, S. Zhu, Z. Li, Y. J. J. o. M. C. A. Liang, *J Mater Chem* **2015**, *3*, 22770; b) C. Nethravathi, A. Dattatreya Manganahalli, M. J. A. A. N. M. Rajamathi, *ACS Appl. Nano Mater.* **2019**, *2*, 2005; c) Q. Qu, B. Liu, J. Liang, H. Li, J. Wang, D. Pan, I. K. Sou, *ACS Catal.* **2020**, *10*, 2656

[17] N. Zhang, F. Zheng, B. Huang, Y. Ji, Q. Shao, Y. Li, X. Xiao, X. Huang, *Adv. Mater.* **2020**, *32*, 1906477.

[18] Q. Jin, S. Jiang, Y. Zhao, D. Wang, J. Qiu, D.-M. Tang, J. Tan, D.-M. Sun, P.-X. Hou, X.-Q. Chen, K. Tai, N. Gao, C. Liu, H.-M. Cheng, X. Jiang, *Nat. Mater.* **2019**, *18*, 62.

[19] N. Gupta, A. Khanna, A.-C. Dippel, O. Gutowski, *RSC Adv.* **2020**, *10*, 13237.

[20] a) B. Jiang, Y. Guo, J. Kim, A. E. Whitten, K. Wood, K. Kani, A. E. Rowan, J. Henzie, Y. Yamauchi, *J. Am. Chem. Soc.* **2018**, *140*, 12434; b) Y. Zhao, M. Luo, S. Chu, M. Peng, B. Liu, Q. Wu, P. Liu, F. M. F. De Groot, Y. Tan, *Nano Energy* **2019**, *59*, 146; c) S. Chen, H. Huang, P. Jiang, K. Yang, J. Diao, S. Gong, S. Liu, M. Huang, H. Wang, Q. Chen, *ACS Catal.* **2019**, *10*, 1152; d) X. Liu, S. Xi, H. Kim, A. Kumar, J. Lee, J. Wang, N. Q. Tran, T. Yang, X. Shao, M. J. N. c. Liang, *Nat. Commun.* **2021**, *12*, 1; e) M. Ji, X. Yang, S. Chang, W. Chen, J. Wang, D. He, Y. Hu, Q. Deng, Y. Sun, B. Li, J. Xi, T. Yamada, J. Zhang, H. Xiao, C. Zhu, J. Li, Y. Li, *Nano Res.* **2022**, *15*, 1959; f) L. Ai, Y. Wang, Y. Luo, Y. Tian, S. Yang, M. Chen, J. Jiang, *J. Alloys Compd.* **2022**, *902*, 163787.